Letter | Editors' Suggestion

Very Large and Reversible Stark-Shift Tuning of Single Emitters in Layered Hexagonal Boron Nitride

Niko Nikolay,[1,2,*] Noah Mendelson,[3] Nikola Sadzak,[1,2] Florian Böhm,[1,2] Toan Trong Tran,[3] Bernd Sontheimer,[1,2] Igor Aharonovich,[3] and Oliver Benson[1,2]

[1] *AG Nanooptik, Humboldt Universität zu Berlin, Newtonstraße 15, D-12489 Berlin, Germany*

[2] *IRIS Adlershof, Humboldt Universität zu Berlin, Zum Großen Windkanal 6, 12489 Berlin, Germany*

[3] *School of Mathematical and Physical Sciences, University of Technology Sydney, Ultimo, New South Wales 2007, Australia*

(Received 11 December 2018; revised manuscript received 17 February 2019; published 15 April 2019)

Combining solid-state single-photon emitters (SPEs) with nanophotonic platforms is a key goal in integrated quantum photonics. In order to realize functionality in potentially scalable elements, suitable SPEs have to be bright, stable, and widely tunable at room temperature. In this work, we show that selected SPEs embedded in a few-layer hexagonal boron nitride (*h*-BN) meet these demands. In order to show the wide tunability of these SPEs we employ an atomic force microscope (AFM) with a conductive tip to apply an electrostatic field to individual *h*-BN emitters sandwiched between the tip and an indium-tin-oxide-coated glass slide. A very large and reversible Stark shift of (5.5 ± 0.3) nm at a zero-field wavelength of 670 nm is induced by applying just 20 V, which exceeds the typical resonance linewidths of nanodielectric and even nanoplasmonic resonators. Our results help to further understand the physical origin of SPEs in *h*-BN as well as for practical quantum photonic applications where wide spectral tuning and on/off resonance switching are required.

DOI: 10.1103/PhysRevApplied.11.041001

I. INTRODUCTION

Bright and tunable solid-state single-photon emitters (SPEs) are required for the realization of scalable quantum photonic technologies [1,2]. Recently, SPEs in hexagonal boron nitride (*h*-BN) have been extensively studied due to their promising optical properties. The *h*-BN SPEs exhibit narrowband linewidths, fast excited-state lifetimes, polarized emission and operate at room temperature, which is attractive for many nanophotonics applications [3–9]. The layered nature of *h*-BN also offers potential advantages for integrating the SPEs with other 2D materials, to achieve hybrid quantum devices based on 2D systems [10–12]. Furthermore, the nanoscale *h*-BN flakes can be coupled with foreign photonic resonators, such as waveguides, microdisks, or photonic crystal cavities, a crucial prerequisite for integrated nanophotonics systems [13,14].

In order to exploit the functionality of a SPE-cavity system, tuning the SPEs' zero phonon line (ZPL) to a cavity's resonance is essential. Therefore, the Stark tuning of various types of SPEs is demonstrated, with, e.g., quantum dots [15,16], color centers in diamond [17,18], defects in WSe_2 [11,19], and defects in MoS_2 [20]. The first works on spectral tuning of *h*-BN SPEs included strain or pressure tuning [21], as well as the application of an electric field by sandwiching the *h*-BN flake between two graphene layers [12,22].

However, at room temperature or for plasmonic resonators switching into and out of resonance requires a reversible and wide-range tuning on the order of one linewidth of such a resonance, which can be as narrow as 17 meV [23,24]. Moreover, state-of-the-art approaches to realize integrated elements for quantum nanophotonics often rely on the identification of precharacterized SPEs and subsequent fabrication of photonic structures around it [25–27]. This requires a procedure to select individual SPEs from a larger ensemble.

In this work, we solve the critical issues mentioned above. We demonstrate the individually controlled and reversible tuning of SPEs in *h*-BN using a high-resolution conductive atomic force microscope (AFM) tip. Using this technique, high fields (up to 5 MV cm^{-1}) can be applied to a nano flake of choice. The few nanometer thickness of *h*-BN is ideal for this method, as the generated electric fields, which are perpendicular to the substrate, are ultimately limited by the distance between the AFM tip and the surface. Under our experimental conditions, we are able to achieve record dynamic tuning of over (5.5 ± 0.3) nm at room temperature.

*nikolay@physik.hu-berlin.de

II. METHODS

In the following, the sample preparation, the experimental setup and a precharacterization are introduced first, followed by a discussion about the measurement of the dipole orientation and the applied electrostatic field strength and direction. Together with a measurement of the E-field-dependent Stark shift, lower limits for dipole moment and polarizability are determined.

A. Sample preparation, experimental setup, and emitter characterization

The sample is prepared by first spin coating a colloidal solution of h-BN flakes (from Graphene Supermarket) onto a sacrificial Si substrate, which is then annealed at 850 °C for 1 h in a 1 mTorr argon atmosphere. Poly(methyl methacrylate) (PMMA) (A5) is then coated on the sample, baked for 5 min at 90 °C, before the PMMA/h-BN film is freed from the substrate by etching in 1 M potassium hydroxide solution. After washing three times in milli-Q water, the sample is then transferred to a prepre-pared indium-tin-oxide- (ITO) coated cover slip, heated to 120 °C to promote adhesion between the h-BN and ITO slide, before the PMMA film is washed away by dissolving in warm acetone overnight, analogous to Ref. [28].

A schematic representation of the experimental setup is shown in Fig. 1(a). A h-BN flake hosting SPEs is sandwiched between a conductive AFM tip and a conductive ITO-coated cover slip. A Solea, PicoQuant laser with a central wavelength of 540 nm (15-nm bandwidth) and a repetition rate of 40 MHz is focused on the SPE from the substrate side via a high-numerical-aperture (1.4) oil-immersion objective lens. SPE fluorescence is then collected by the same lens, passed through a 610-nm long-pass filter, an optional confocal pinhole, and finally guided either into a spectrometer, a Hanbury Brown and Twiss (HBT) interferometer, or an EMCCD camera recording a real or a Fourier image of the sample plane. Without saturating the emitter to prevent photobleaching, a count rate of 75 10^3 counts/s is detected by the avalanche photodiodes (APDs). A PL lifetime measurement (shown within the Supplemental Material [29]) revealed an excited-state lifetime of $\tau_{h\text{-BN}} = (4.82 \pm 0.01)$ ns, which is in the expected range for SPEs in h-BN [30]. Since the linear Stark shift depends on the alignment of the dipole moment of the emitter with respect to the electrostatic field direction, we must ensure that only the shift of the ZPL of a single emitter with known orientation is investigated. Thus, a second order correlation [$g^{(2)}$] function is calculated from photon arrival times recorded in the HBT setup. Blue dots in Fig. 1(c) represent the $g^{(2)}$ function. The antibunching at $\tau = 0$ is below 0.5 and thus the emission can be considered as a predominantly single-photon stream resulting from a SPE.

B. Electrostatic field between tip and ITO layer

In order to identify the field strength and direction experienced by the SPE, the electrostatic field distribution present in the conducted experiment is simulated using COMSOL Multiphysics. As parameters for the simulation, an AFM tip radius of 30 nm, a tip to ITO surface distance of 125 nm (measured with the AFM), a h-BN permittivity of 4 [31], and a voltage of 20 V are set. Figure 1(b) shows the field strength and direction indicated by the color coding and the arrows, respectively. The exact SPE position within the h-BN flake is unknown, but two assumptions

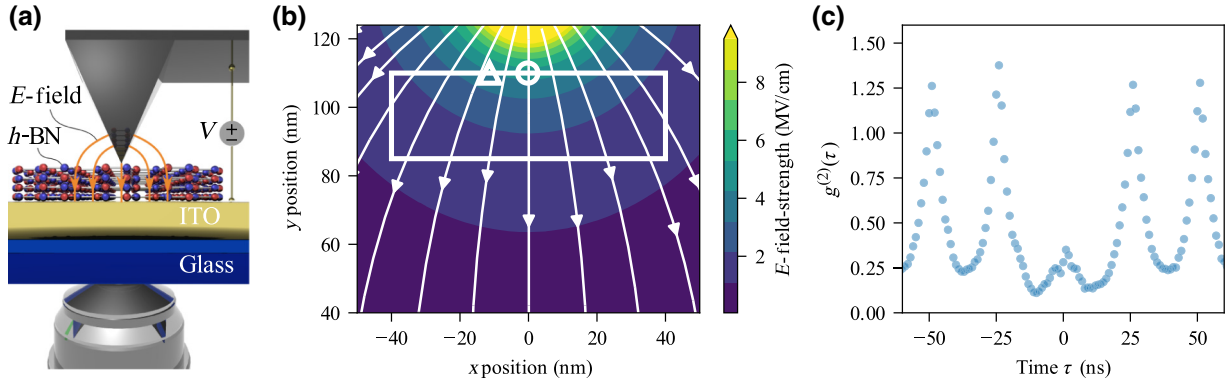

FIG. 1. Schematic representation of the experiment, electrostatic field distribution and $g^{(2)}$ function. (a) An h-BN flake is located on an ITO-covered glass substrate. The oil-immersion objective lens below excites the h-BN SPE and collects its emission as an AFM tip can be used to deliver an electrostatic field causing a Stark shift of the ZPL. (b) The electrostatic field strength between the AFM tip (h-BN starts at $y = 125$ nm) and ITO (starts at $y = 0$) caused by the application of 20 V is represented by the contour diagram. The superimposed stream flow chart shows the field orientation. The assumed SPE position (discussed in the text) is marked by the white rectangle. Points with the highest $|\vec{\mu}\vec{E}|$ and $|\vec{E}|^2$ within the assumed SPE area are marked by the triangle and the circle, respectively. (c) The second-order autocorrelation of the emitters' fluorescence [$g^{(2)}(\tau)$] shows a clear antibunching at $\tau = 0$ that indicates for primarily single-photon emission.

can be made to reduce the possible residence volume marked by the white rectangle. When the approached tip is scanned over the SPE, an intensity drop of up to 20% is observed. This drop is expected as the AFM tip alters the SPE radiation pattern, as well as the tip providing plasmonic decay channels potentially decreasing the external quantum efficiency. Simulations shown within the Supplemental Material [29] map the decrease in intensity to a SPE depth below the *h*-BN flake surface. The experimentally obtained drop is reproduced by the simulation at a minimal depth of 15 nm. Furthermore, a noticeable Stark shift could only be seen when the lateral tip position is within an area of 40 nm in diameter. At the edge of this area, the electric field strength should be at least halved compared to its maximum in the center in order to quarter a quadratic Stark shift, rendering any shift in the experiment invisible by the naked eye. This leads to a maximal depth of 40 nm. Just the volume within those constraints [marked by the white rectangle in Fig. 1(b)] is considered in the following discussions.

C. Dipole-orientation measurement

Next, we discuss the extraction of the dipole orientation from polarization-dependent intensity measurements, which is crucial to determine the vectorial SPE dipole moment. Two angles, the in-plane angle ϕ and the out-of-plane angle θ fully characterize its orientation. To determine both angles, a polarimetric measurement is performed [32]. The horizontal and vertical polarization components of the SPE fluorescence are spatially separated using a polarizing beam splitter (PBS) and then individually detected via APDs at the corresponding output port of the beam splitter. A $\lambda/2$ plate before the PBS enables us to rotate the SPE polarization by the angle α. To correct for intensity variations of the SPE during the measurement as well as for different detection efficiencies of each APD, we calculate the relative amount of the intensity detected by one APD as shown in Eq. (S3) within the Supplemental Material [29]. The inset of Fig. 2(a) shows the resulting portion of the detected signal (dots), and a fit (line) of the following formula [32]:

$$f(\alpha) = I_{\min} + (I_{\min} - I_{\max}) \sin^2(\alpha + \phi), \qquad (1)$$

with the fit parameters $I_{\min} = (0.262 \pm 0.003)$ arb. units, $I_{\max} = (0.740 \pm 0.005)$ arb. units and the in-plane angle $\phi = (52.9 \pm 0.2)^\circ$. The degree of polarization, given by $\delta = (I_{\max} - I_{\min})/(I_{\max} + I_{\min})$, is related to the out-of-plane angle θ. We simulate a dipole with an orientation given by ϕ and θ, located in a *h*-BN flake (125 nm in diameter, measured with the AFM) on top of a glass cover slide with JCM wave, a 3D finite-element Maxwell solver [33]. From this simulation, we extract the degree of polarization δ for any θ and compare it with the measured data, shown in Fig. 2(a), a detailed discussion can be found within the Supplemental Material [29]. In this way, we determine $\theta = (59.9 \pm 0.2)^\circ$. To verify whether the simulated geometry is suitable to model the present experimental conditions, we quantitatively compare a simulated with a measured Fourier image, shown in Figs. 2(b) and 2(c), respectively. The dipole orientation in the simulation is given by the just-determined angles ϕ and θ, no free parameters are used. A clear similarity of both Fourier images is seen.

D. Determining the resonance energy

To quantify relative spectral shifts, the ZPL central energy is determined. In order to account for the asymmetric nature of the ZPL at room temperature, resulting from acoustic phonons [3], we fit a sum of two Lorentzian distributions. Fit parameters and the fitted distribution function are shown within the Supplemental Material [29]. Figure 3(a) shows PL spectra from the sandwiched SPE in

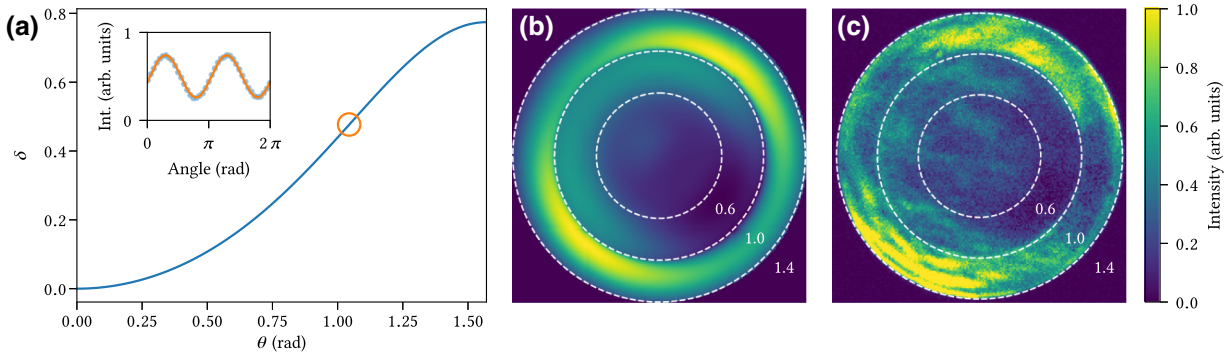

FIG. 2. Determination of the dipole orientation. (a) Simulated degree of polarization δ with respect to the dipole out-of-plane angle θ. The orange circle represents the measured δ. In the inset, a corresponding polarization measurement of the fluorescence light (dots) and a fit (solid line) is shown. The signal is normalized to the total intensity detected by both APDs and corrected for its different detection efficiencies. (b) Simulated Fourier image with a dipole orientation of $\theta = (59.9 \pm 0.2)^\circ$ and $\phi = (52.9 \pm 0.2)^\circ$ determined by the polarization measurement shown in (a). (c) Fourier image of the SPE taken with a NA = 1.4 objective lens. The striking similarity between (b) and (c) proves that the simulation is suited to derive the experimental results very well.

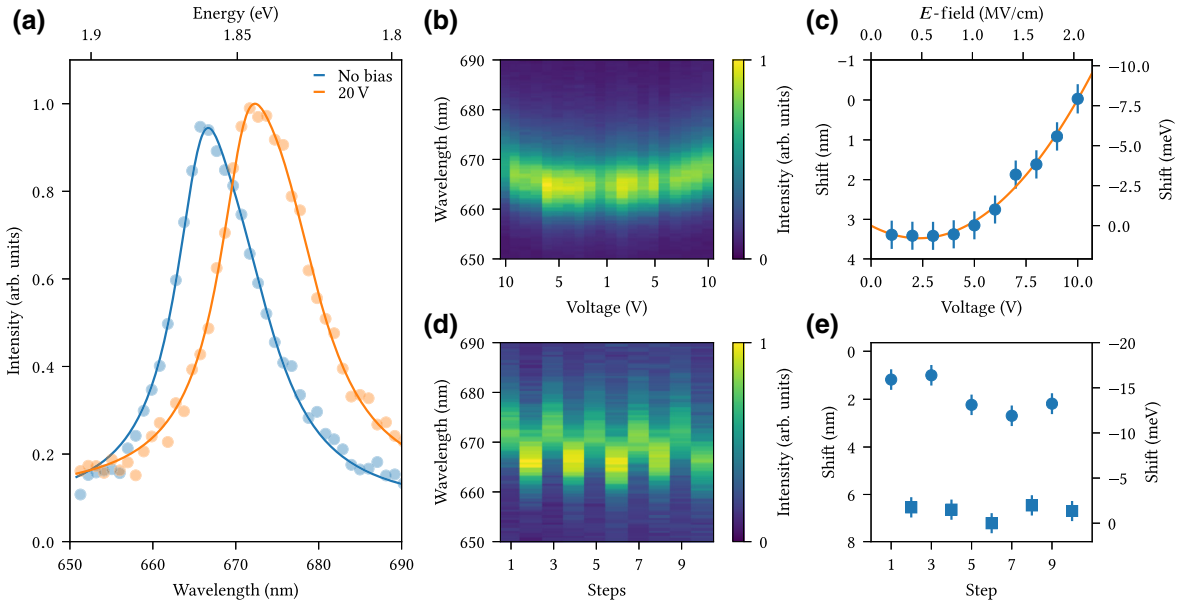

FIG. 3. Spectra of the Stark-shifted *h*-BN SPE fluorescence. (a) Measured spectra and corresponding fits of the unshifted emission in blue (left peak) and shifted in orange (right peak), taken with an integration time of 2.5 s and binned to 1-nm bins. This shift of (5.9 ± 0.6) nm is recorded with a tip to substrate distance of approximately 125 nm and a voltage of 20 V. (b) *h*-BN-ZPL spectra recorded while the electric field strength between tip and ITO layer is lowered and increased again (from left to right, in 1-V steps). (c) Blue dots are spectral shifts determined by fits of Eq. (S4) within the Supplemental Material [29] to the data shown in (b). The solid line shows Eq. (2) that is fit to the data points. (d) Spectra recorded while a voltage of 20 V is switched on and off. (e) Spectral shifts determined by fits to the data in (d) show an average shift of (5.5 ± 0.3) nm [(15.4 ± 0.8) meV].

few-layer *h*-BN (dots) and corresponding fits (solid lines) without voltage (blue) and 20 V (orange) applied. A clear shift of (5.9 ± 0.6) nm can be quantified in this way.

III. RESULTS

We now proceed to study in detail the Stark-shift behavior and the modulation of the emission. Figure 3(b) shows the ZPL spectra of a SPE as a function of the applied voltage. This experiment is done without readjusting the tip position, each spectrum is recorded for 5 s. First, the voltage is reduced, resulting in a blue-shifted emission. Then, the voltage is increased back to its initial value, resulting in a red shift back to the original ZPL central energy, which indicates for a fully reversible shift. Fits of the double Lorentzian distribution to the averaged spectra (i.e., spectra taken at the same voltage are averaged) reveal central energies with respect to the applied voltage, shown in Fig. 3(c) as relative shifts. From this, we determine the dipole moment μ and the polarizability α by fitting the following formula adapted from Refs. [12,34,35]:

$$\Delta(\hbar\omega) = -|\vec{\mu}||\vec{E}|\cos[\angle(\vec{\mu},\vec{E})] - \frac{1}{2}\alpha|\vec{E}|^2. \qquad (2)$$

For this, the applied voltage must be related to an electric field seen by the SPE. As discussed before, the exact SPE position is unknown, and thus we are limited to estimating the minimum values for $|\vec{\mu}|$ and α. Two points in the electrostatic vector field [represented in Fig. 1(b)] are selected to relate the voltage to the electric field: one at which the scalar product $|\vec{\mu}\vec{E}|$ is maximum [marked by a triangle in Fig. 1(b)] and one at which $|\vec{E}|^2$ is maximum (marked by a circle). The direction of $\vec{\mu}$ is given by the previously determined dipole orientation. At each point, a minimum value is determined by fitting Eq. (2) to the data points, where the x axis is scaled for each maximum point according to the E-field simulation. In Fig. 3(c), the upper x axis is exemplary scaled for the case of minimal $|\vec{\mu}|$, i.e., the triangle in Fig. 1(b). The minimum values are given by $|\vec{\mu}|_{\mathrm{min}} = (2.1 \pm 0.2)$ D, corresponding to a charge separation of $r_{\mathrm{min}} = (0.44 \pm 0.04)$ Å (with $|\vec{\mu}|_{\mathrm{min}} = e\, r_{\mathrm{min}}$) and $\alpha_{\mathrm{min}} = (770 \pm 50)$ Å^3, both given in centimeter-gram-second system of units. They are in contrast to what was stated in the literature for *h*-BN Stark tuning, where maximum values were given by $|\vec{\mu}|_{\mathrm{lit}} = 0.9$ D and $\alpha_{\mathrm{lit}} = 150$ Å^3 [12]. The discrepancy may result from the different dipole orientation with respect to the electric field, or the SPEs are of different atomic origin.

Finally, we demonstrate the reversibility of the shift and the stability of the emission over ten cycles. For this purpose, we apply a square wave voltage between the AFM tip and the ITO layer with an amplitude of 20 V, a 50% duty cycle, and a period time of 5 s. Note that the AFM tip position is fixed during the whole measurement run. Again, the emission spectrum is recorded during this experiment, shown in Fig. 3(d). As before, fitting the double Lorentzian

distribution to these spectra gives central positions shown in Fig. 3(e) as relative shifts. A reversible shift of (5.5 ± 0.3) nm [(15.4 ± 0.8) meV] in average is observed over ten cycles. In the performed experiment, the ultimate limitation of the switching speed is given by the capacitance of the capacitor formed by the ITO surface and the AFM tip. With the analytical model described in Ref. [36] and our instrument-specific parameters shown in Ref. [37], the estimated capacity of our system is $C \approx 6$ fF.

A possible application of the examined method could be the accurate determination of the SPE position. Once the dipole orientation and the electric-field-dependent Stark shift are determined, it would be possible to calculate at which lateral tip SPE displacement the highest Stark shift is found. By scanning the tip while simultaneously monitoring the Stark shift and the topography, the SPE position can be determined accurately.

IV. SUMMARY

In summary, we sandwich a *h*-BN flake hosting SPEs between a transparent conductive ITO layer and a conductive AFM tip. By applying a voltage between the two, a very large reversible Stark shift of (5.5 ± 0.3) nm [(15.4 ± 0.8) meV] exceeding the resonance linewidth of typical nanodielectric and nanoplasmonic resonators [23,38] is observed. Determining the SPE dipole orientation, its approximate position with respect to the AFM tip, and the electrostatic field distribution allowed us to translate the applied voltage into a vectorial electrostatic field experienced by the SPE. We find a linear and a quadratic Stark shift, described by the dipole moment of $|\vec{\mu}|_{\text{min}} = (2.1 \pm 0.2)$ D and the polarizability of $\alpha_{\text{min}} = (770 \pm 50)$ Å^3. We could show that this very large Stark shift of the ZPL line is reversible and can be applied arbitrarily. This displays the potential to integrate selected SPEs in *h*-BN in bisected plasmonic resonators, such as nanoparticle-on-metal plasmonic antennas [39]. Such a configuration would represent a tunable plasmonic cavity quantum electrodynamical system at room temperature.

ACKNOWLEDGMENTS

Financial support from the German Ministry of Education and Research (BMBF) project "NANO-FILM," the Australian Research council (via Grant No. DP180100077), the Asian Office of Aerospace Research and Development Grant No. FA2386-17-1-4064, the Office of Naval Research Global under Grant No. N62909-18-1-2025 are gratefully acknowledged. I.A. is grateful for the Humboldt Foundation for their generous support. O.B. acknowledges the UTS Distinguished Visiting Scholars scheme.

[1] David D. Awschalom, Ronald Hanson, Jörg Wrachtrup, and Brian B. Zhou, Quantum technologies with optically interfaced solid-state spins, Nat. Photonics **12**, 516 (2018).

[2] Mete Atatüre, Dirk Englund, Nick Vamivakas, Sang-Yun Lee, and Joerg Wrachtrup, Material platforms for spin-based photonic quantum technologies, Nat. Rev. Mater. **3**, 38 (2018).

[3] Nicholas R. Jungwirth, Brian Calderon, Yanxin Ji, and Michael G. Spencer, Temperature dependence of wavelength selectable zero-phonon emission from single defects in hexagonal boron nitride, Nano Lett. **16**, 6052 (2016).

[4] L. J. Martínez, T. Pelini, V. Waselowski, J. R. Maze, B. Gil, G. Cassabois, and V. Jacques, Efficient single photon emission from a high-purity hexagonal boron nitride crystal, Phys. Rev. B **94**, 121405(R) (2016).

[5] Toan Trong Tran, Kerem Bray, Michael J. Ford, Milos Toth, and Igor Aharonovich, Quantum emission from hexagonal boron nitride monolayers, Nat. Nanotechnol. **11**, 37 (2016).

[6] Bernd Sontheimer, Merle Braun, Niko Nikolay, Nikola Sadzak, Igor Aharonovich, and Oliver Benson, Photodynamics of quantum emitters in hexagonal boron nitride revealed by low-temperature spectroscopy, Phys. Rev. B **96**, 121202(R) (2017).

[7] Mehran Kianinia, Blake Regan, Sherif Abdulkader Tawfik, Toan Trong Tran, Michael J. Ford, Igor Aharonovich, and Milos Toth, Robust solid-state quantum system operating at 800 K, ACS Photonics **4**, 768 (2017).

[8] Noah Mendelson, Zai-Quan Xu, Toan Trong Tran, Mehran Kianinia, John Scott, Carlo Bradac, Igor Aharonovich, and Milos Toth, Engineering and tuning of quantum emitters in few-layer hexagonal boron nitride, ACS Nano **13**, 3132 (2019).

[9] Annemarie L. Exarhos, David A. Hopper, Raj N. Patel, Marcus W. Doherty, and Lee C. Bassett, Magnetic-field-dependent quantum emission in hexagonal boron nitride at room temperature, Nat. Commun. **10**, 222 (2019).

[10] Achim Woessner, Mark B. Lundeberg, Yuanda Gao, Alessandro Principi, Pablo Alonso-González, Matteo Carrega, Kenji Watanabe, Takashi Taniguchi, Giovanni Vignale, Marco Polini, James Hone, Rainer Hillenbrand, and Frank H. L. Koppens, Highly confined low-loss plasmons in graphene–boron nitride heterostructures, Nat. Mater. **14**, 421 (2015).

[11] Chitraleema Chakraborty, Kenneth M. Goodfellow, Sajal Dhara, Anthony Yoshimura, Vincent Meunier, and A. Nick Vamivakas, Quantum-confined Stark effect of individual defects in a van der Waals heterostructure, Nano Lett. **17**, 2253 (2017).

[12] Gichang Noh, Daebok Choi, Jin-Hun Kim, Dong-Gil Im, Yoon-Ho Kim, Hosung Seo, and Jieun Lee, Stark tuning of single-photon emitters in hexagonal boron nitride, Nano Lett. **18**, 4710 (2018).

[13] Nasim Alem, Rolf Erni, Christian Kisielowski, Marta D. Rossell, Will Gannett, and A. Zettl, Atomically thin hexagonal boron nitride probed by ultrahigh-resolution transmission electron microscopy, Phys. Rev. B **80**, 155425 (2009).

[14] Nicholas V. Proscia, Zav Shotan, Harishankar Jayakumar, Prithvi Reddy, Charles Cohen, Michael Dollar, Audrius Alkauskas, Marcus Doherty, Carlos A. Meriles, and Vinod M. Menon, Near-deterministic activation of

room-temperature quantum emitters in hexagonal boron nitride, Optica **5**, 1128 (2018).

[15] Raj B. Patel, Anthony J. Bennett, Ian Farrer, Christine A. Nicoll, David A. Ritchie, and Andrew J. Shields, Two-photon interference of the emission from electrically tunable remote quantum dots, Nat. Photonics **4**, 632 (2010).

[16] A. K. Nowak, S. L. Portalupi, V. Giesz, O. Gazzano, C. Dal Savio, P.-F. Braun, K. Karrai, C. Arnold, L. Lanco, I. Sagnes, A. Lemaître, and P. Senellart, Deterministic and electrically tunable bright single-photon source, Nat. Commun. **5**, 3240 (2014).

[17] Ph. Tamarat, T. Gaebel, J. R. Rabeau, M. Khan, A. D. Greentree, H. Wilson, L. C. L. Hollenberg, S. Prawer, P. Hemmer, F. Jelezko, and J. Wrachtrup, Stark shift control of single optical centers in diamond, Phys. Rev. Lett. **97**, 083002 (2006).

[18] T. Müller, I. Aharonovich, L. Lombez, Y. Alaverdyan, A. N. Vamivakas, S. Castelletto, F. Jelezko, J. Wrachtrup, S. Prawer, and M. Atatüre, Wide-range electrical tunability of single-photon emission from chromium-based colour centres in diamond, New J. Phys. **13**, 075001 (2011).

[19] S. Schwarz, A. Kozikov, F. Withers, J. K. Maguire, A. P. Foster, S. Dufferwiel, L. Hague, M. N. Makhonin, L. R. Wilson, A. K. Geim, K. S. Novoselov, and A. I. Tartakovskii, Electrically pumped single-defect light emitters in WSe2, 2D Mater. **3**, 25038 (2016).

[20] Julian Klein, Jakob Wierzbowski, Armin Regler, Jonathan Becker, Florian Heimbach, K. Müller, Michael Kaniber, and Jonathan J. Finley, Stark effect spectroscopy of mono- and few-layer MoS2, Nano Lett. **16**, 1554 (2016).

[21] Yongzhou Xue, Hui Wang, Qinghai Tan, Jun Zhang, Tongjun Yu, Kun Ding, Desheng Jiang, Xiuming Dou, Jun-jie Shi, and Bao-quan Sun, Anomalous pressure characteristics of defects in hexagonal boron nitride flakes, ACS Nano **12**, 7127 (2018).

[22] Gabriele Grosso, Hyowon Moon, Benjamin Lienhard, Sajid Ali, Dmitri K. Efetov, Marco M. Furchi, Pablo Jarillo-Herrero, Michael J. Ford, Igor Aharonovich, and Dirk Englund, Tunable and high-purity room temperature single-photon emission from atomic defects in hexagonal boron nitride, Nat. Commun. **8**, 705 (2017).

[23] Shunping Zhang and Hongxing Xu, Tunable dark plasmons in a metallic nanocube dimer: toward ultimate sensitivity nanoplasmonic sensors, Nanoscale **8**, 13722 (2016).

[24] Rohit Chikkaraddy, Bart de Nijs, Felix Benz, Steven J. Barrow, Oren A. Scherman, Edina Rosta, Angela Demetriadou, Peter Fox, Ortwin Hess, and Jeremy J. Baumberg, Single-molecule strong coupling at room temperature in plasmonic nanocavities, Nature **535**, 127 (2016).

[25] Q. Shi, B. Sontheimer, N. Nikolay, A. W. Schell, J. Fischer, A. Naber, O. Benson, and M. Wegener, Wiring up pre-characterized single-photon emitters by laser lithography, Sci. Rep. **6**, 31135 (2016).

[26] M. Gschrey, F. Gericke, A. Schüßler, R. Schmidt, J.-H. Schulze, T. Heindel, S. Rodt, A. Strittmatter, and S. Reitzenstein, *In situ* electron-beam lithography of deterministic single-quantum-dot mesa-structures using low-temperature cathodoluminescence spectroscopy, Appl. Phys. Lett. **102**, 251113 (2013).

[27] A. Dousse, L. Lanco, J. J. Suffczyński, E. Semenova, A. Miard, A. Lemaître, I. Sagnes, C. Roblin, J. Bloch, and P. Senellart, Controlled Light-Matter Coupling for a Single Quantum Dot Embedded in a Pillar Microcavity Using Far-Field Optical Lithography, Phys. Rev. Lett. **101**, 267404 (2008).

[28] Toan Trong Tran, Danqing Wang, Zai-Quan Xu, Ankun Yang, Milos Toth, Teri W. Odom, and Igor Aharonovich, Deterministic coupling of quantum emitters in 2D materials to plasmonic nanocavity arrays, Nano Lett. **17**, 2634 (2017).

[29] See Supplemental Material at http://link.aps.org/supplemental/10.1103/PhysRevApplied.11.041001 for description of the lifetime measurement, the determination of the dipole – AFM tip distance, the normalization of the polarization intensity, the function and fit values used to fit the recorded spectra, and the spectral shifts of another single-photon emitter in *h*-BN.

[30] Toan Trong Tran, Christopher Elbadawi, Daniel Totonjian, Charlene J. Lobo, Gabriele Grosso, Hyowon Moon, Dirk R. Englund, Michael J. Ford, Igor Aharonovich, and Milos Toth, Robust multicolor single photon emission from point defects in hexagonal boron nitride, ACS Nano **10**, 7331 (2016).

[31] Terence E. Warner, *Synthesis, Properties and Mineralogy of Important Inorganic Materials* (John Wiley & Sons, Ltd, Chichester, UK, 2011), p. 550.

[32] Clotilde Lethiec, Julien Laverdant, Henri Vallon, Clémentine Javaux, Benoît Dubertret, Jean-Marc Frigerio, Catherine Schwob, Laurent Coolen, and Agnès Maître, Measurement of Three-Dimensional Dipole Orientation of a Single Fluorescent Nanoemitter by Emission Polarization Analysis, Phys. Rev. X **4**, 021037 (2014).

[33] JCMwave GmbH: JCM wave (2018).

[34] P. W. Fry, I. E. Itskevich, D. J. Mowbray, M. S. Skolnick, J. J. Finley, J. A. Barker, E. P. O'Reilly, L. R. Wilson, I. A. Larkin, P. A. Maksym, M. Hopkinson, M. Al-Khafaji, J. P. R. David, A. G. Cullis, G. Hill, and J. C. Clark, Inverted Electron-Hole Alignment in InAs-GaAs Self-Assembled Quantum Dots, Phys. Rev. Lett. **84**, 733 (2000).

[35] J. A. Barker and E. P. O'Reilly, Theoretical analysis of electron-hole alignment in InAs-GaAs quantum dots, Phys. Rev. B **61**, 13840 (2000).

[36] J. Colchero, A. Gil, and A. M. Baró, Resolution enhancement and improved data interpretation in electrostatic force microscopy, Phys. Rev. B **64**, 245403 (2001).

[37] Niko Nikolay, Nikola Sadzak, Alexander Dohms, Boaz Lubotzky, Hamza Abudayyeh, Ronen Rapaport, and Oliver Benson, Accurate placement of single nanoparticles on opaque conductive structures, Appl. Phys. Lett. **113**, 113107 (2018).

[38] Mikhail V. Rybin, Kirill L. Koshelev, Zarina F. Sadrieva, Kirill B. Samusev, Andrey A. Bogdanov, Mikhail F. Limonov, and Yuri S. Kivshar, High-Q Supercavity Modes in Subwavelength Dielectric Resonators, Phys. Rev. Lett. **119**, 243901 (2017).

[39] Bart de Nijs, Richard W. Bowman, Lars O. Herrmann, Felix Benz, Steve J. Barrow, Jan Mertens, Daniel O. Sigle, Rohit Chikkaraddy, Anna Eiden, Andrea Ferrari, Oren A. Scherman, and Jeremy J. Baumberg, Unfolding the contents of sub-nm plasmonic gaps using normalising plasmon resonance spectroscopy, Faraday Discuss. **178**, 185 (2015).